Volume 12 | Number 21 | 7 November 2025

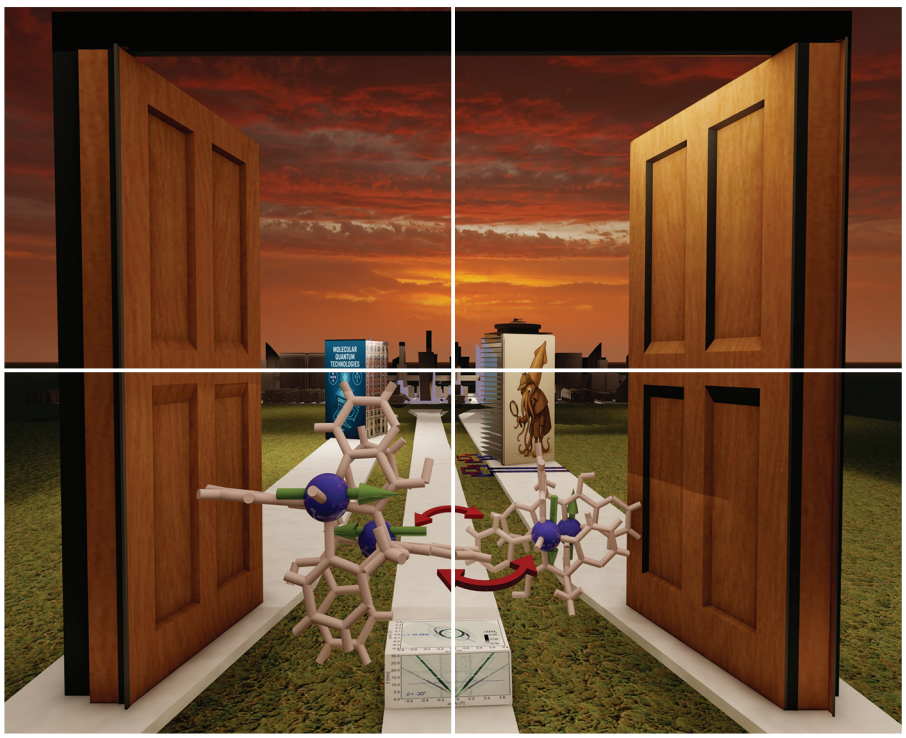

INORGANIC CHEMISTRY

FRONTIERS

CCS 中国化学会 CHINESE CHEMICAL SOCIETY
PEKING UNIVERSITY 1898
ROYAL SOCIETY OF CHEMISTRY
rsc.li/frontiers-inorganic

INORGANIC CHEMISTRY
FRONTIERS

RESEARCH ARTICLE

View Article Online
View Journal | View Issue

Cite this: *Inorg. Chem. Front.*, 2025, **12**, 6460

From strong to weak interaction: reconciling SQUID and μSQUID-EPR data in anomalous Co(II) dimers

Sagar Paul, *[a] Malay Dolai, *[b] Juli Nanda Goswami,[b] Biswajit Bhattacharya, [c] Franziska Emmerling, [c] Michael G. B. Drew, [d] Shouvik Chattopadhyay, *[e] Rabi Sankar Sarkar, [e] Appu Sunil,[a] Ghenadie Novitchi,[f] Eufemio Moreno-Pineda *[a,g,h] and Wolfgang Wernsdorfer *[a,i]

Magnetic molecules have been proposed as scaffolds for novel quantum technologies, ranging from quantum sensing and quantum memory to multilevel quantum bits (qudits) and fault-tolerant quantum computation. Integration of magnetic molecules into cutting-edge applications hinges on a deep understanding and tunability of their spin states. To date, the strategic manipulation of the local environment of the ion and careful selection of the magnetic core have enabled the desired tunability and scalability of the spin states. For such goals, however, extracting the anisotropic parameters that dictate the characteristics of the Spin Hamiltonian is challenging, especially for molecules consisting of multiple magnetic cores. We address these challenges by studying two cobalt(II) dinuclear systems, complicated by inherent spin–orbit coupling. We explore the magnetic properties of these systems in two temperature regimes: (i) at sub-Kelvin temperatures employing single crystals at 30 mK using a unique μSQUID-EPR technique that examines the microwave absorption peaks in the magnetisation data and their variation with field angle and frequency; and (ii) in bulk employing convectional SQUID magnetometry above 2 K *i.e.*, $\chi_M T(T)$ and $M(H)$. Unexpectedly, sub-Kelvin temperature investigations reveal a negligible interaction, whereas the SQUID data reveal a much stronger interaction between the Co(II) ions. An understanding of these data is developed based on a strong coupling model and the coupling of two moieties with a spin-effective ground state.

Received 27th June 2025,
Accepted 21st August 2025

DOI: 10.1039/d5qi01387a

rsc.li/frontiers-inorganic

Introduction

Magnetic molecules (MMs) are attractive quantum objects, proposed as platforms for emerging quantum technologies.[1–4] Engineering the ligand field, magnetic cores, and incorporating nuclear spins of the magnetic ion can provide great control over the tunability and scalability of the spins. Employing such an approach, it has been possible to design MMs with the desired characteristics.[5,6] The remarkable control gained over these systems has opened the door to many new possibilities, such as high-density storage and quantum computing, among others.[1–4,7,8] On the data storage side, the significant control over the tunability has led to surpassing the liquid-nitrogen temperature limit,[9] while it has also been possible to create dimeric units to operate as quantum gates[10–12] or for quantum error correction protocols,[13,14] the engineering of noise-resilient qubits,[15–17] and even the execution of a quantum algorithm.[18] These advances make MMs excellent testbeds for more advanced quantum technology schemes.[2–4,7] For example, the multilevel character of these systems has been proposed as qudits,[3,19] which may outperform qubits in

[a]*Physikalisches Institut, Karlsruhe Institute of Technology, D-76131 Karlsruhe, Germany. E-mail: sagar.paul@kit.edu, eufemio.moreno@up.ac.pa, wolfgang.wernsdorfer@kit.edu*
[b]*Department of Chemistry, Prabhat Kumar College, Purba Medinipur 721404, West Bengal, India. E-mail: dolaimalay@yahoo.in*
[c]*BAM Federal Institute for Materials Research and Testing, Richard-Willstätter-Str. 11 12489, Berlin, Germany*
[d]*School of Chemistry, The University of Reading, P.O. Box 224, Whiteknights, Reading RG6 6AD, UK*
[e]*Department of Chemistry, Jadavpur University, Kolkata - 700032, India. E-mail: shouvik.chem@gmail.com*
[f]*Laboratoire National des Champs Magnétiques Intenses, UPR CNRS 3228, Université Grenoble-Alpes, B.P. 166, 38042 Grenoble Cedex 9, France*
[g]*Universidad de Panamá, Facultad de Ciencias Naturales, Exactas y Tecnología, Depto. de Química-Física, 0824 Panamá, Panamá*
[h]*Universidad de Panamá, Facultad de Ciencias Naturales, Exactas y Tecnología, Grupo de Investigación de Materiales, 0824 Panamá, Panamá*
[i]*Institute for Quantum Materials and Technology (IQMT), Karlsruhe Institute of Technology (KIT), Eggenstein-Leopoldshafen D-76344, Germany*

quantum information processing schemes. Moreover, they can be employed directly to perform quantum algorithms[18] or quantum error correction protocols.[13,20,21]

However, to successfully incorporate MMs into quantum technologies, a detailed understanding of the electronic characteristics of these systems is required. To this end, several techniques have proven resourceful in determining the physical parameters governing the quantum characteristics of the systems. Experimentally, above 2 K, the bulk magnetic parameters are commonly investigated through SQUID magnetometry,[22,23] Electron Paramagnetic Resonance (EPR) spectroscopy,[24–27] magnetic far infrared,[23,28] and torque magnetometry,[27,29] among others.[30] In a combinatorial approach, these techniques are often interconnected with wave function-based theoretical routes for the complete understanding of the spin system.[31–33] Furthermore, new theoretical approaches have shed light on the relaxation characteristics of these systems, hence providing new playgrounds to fine-tune their magnetic characteristics.[5,34] But even with these approaches, certain crucial parameters like those pertaining to the magnetic anisotropy and intra-molecular interaction proved difficult to obtain. Thus, moving forward, the development of improved techniques is critical. Recently, some of us have shown that by merging two highly sensitive techniques, such as μSQUID magnetometry and EPR spectroscopy, many of the highly elusive crystal field parameters for lanthanide-based MMs can be extracted.[35] These studies are performed at sub-Kelvin temperatures, allowing the precise determination of the spin Hamiltonian parameters of the ground states. Here, to deepen our understanding of MMs, and as a further exploitation of the sensitivity of the μSQUID-EPR technique, we investigate two cobalt Co(II)-complexes dimers in two regimes, that is, from room temperature to 2 K, through SQUID magnetometry and at 30 mK sub-Kelvin temperature, *via* μSQUID-EPR.

Co(II) in octahedral symmetry, is one of the most difficult-to-understand ions in the 3d transition metal row.[24,36–40] The magnetic anisotropy in Co(II) ions in octahedral symmetry and its inherent spin–orbit coupling, intrinsic to this ion in cubic symmetry, often precludes their spin Hamiltonian characterisation. Although the relaxation dynamics of these systems are far from ideal from a qubit/qudit perspective, a salient characteristic of the systems herein studied is that the magnetic hysteresis loops measured by μSQUID alone provide very little information about the magnetic characteristics of the systems. In contrast, the μSQUID-EPR technique allows direct exploration of the spin states by coupling microwaves to the crystal by a coplanar waveguide and *in situ* magnetisation measurement. The technique examines the microwave absorption peaks in the magnetisation data and their variation with field-angle and frequency. It enables the exploration of the field-angle and microwave-frequency (1–30 GHz) dependent absorption maps extracted from magnetic hysteresis loops at cryostat temperatures down to 30 mK. Simulation of the angular and frequency maps affords the entire spin Hamiltonian for both systems. A stark difference is found between the conventional SQUID magnetometry data and the μSQUID-EPR loops pertaining to the operative interaction in the dimers. Through detailed analysis, supported by theoretical calculations, we resolved the discrepancy by identifying the coexistence of two distinct components in the samples: one strongly coupled and the other weakly coupled. Such coexistence of multiple interactions has been observed often in multi-nuclear molecular systems,[41,42] however, using the angle and frequency dependent EPR study, here we are able to pinpoint the orientations and magnitude of interactions of the weakly interacting components, even though a strong interaction persists in the dimeric systems. As a result, we show how in a combinatorial approach, both magnetic and spectroscopic data allow the understanding of the magnetic characteristics of MMs.

Results

Structural characteristics of Co(II) dimers

Two Co(II) dimers were selected for the study. The first dimeric complex is a mixed valence tetranuclear cobalt complex with the formula $[(\mu_{1,1}\text{-}N_3)\{Co^{II}(L^r)(\mu\text{-}O_2CR)Co^{III}(N_3)\}_2]ClO_4{\cdot}H_2O{\cdot}1.5CH_3OH$ where H_2L^r = [(1,3-propanediyl)bis(iminomethylene)bis(6-methoxyphenol)], RCO_2H = 4-methyl-3-nitrobenzoic acid (Fig. 1a). Although the complex bears four cobalt ions, the non-magnetic nature of the two Co(III) centres renders a magnetic dimeric Co(II) system. From here on, we refer to this complex as **1Co$_2$** (synthetic details are given in section A.1 in the SI). Crystallographic studies show that **1Co$_2$** crystallises in the triclinic $P\bar{1}$ space group, with two inversion-related molecules residing in the unit cell (Fig. S5). The Co(II)···N for both Co(II) ions in **1Co$_2$** are found to be 2.063(2) Å and 2.062(3) Å. Likewise, both Co(II) ions are bridged by an azide group, which can act as a spin carrier between the ions. The Co(II)···Co(II) distance is found to be 3.7862(5) Å Co(II)···Co(II), with a Co(II)···N···Co(II) bond angle of 133.2(1)°. Based on the large Co(II)···N···Co(II) bond angle, ferromagnetic interactions are deemed possible. In the packing, the shortest Co(II)···Co(II) distance is found to be 11.0439(6) Å; hence, intermolecular interactions are expected to be negligible.

The second system is a dinuclear system with the formula $[Co^{II}(L)_2(Cl)_2]Cl_2$ where L = *N*-(methoxy(pyrimidin-2-yl)(pyrimidine-2-carboxamido)methyl)(pyrimidine-2-carboxamide), here on termed as **2Co$_2$** (Fig. 1b) (details are given in section A.2 of the SI). **2Co$_2$** crystallises in a monoclinic unit cell with *C*2/*c* with four molecules residing in the unit cell, with two different orientations (Fig. S6). In contrast to **1Co$_2$**, where a N_3^- ligand acts as a direct bridge between the Co(II) ions, in **2Co$_2$**, the Co(II) ions are bridged by the L ligand, providing no direct contact between the metals. The Co(II)···Co(II) distance in this system is found to be 5.5632(7) Å, much longer than the one observed in **1Co$_2$**. Detailed crystallographic parameters and further structural characteristics for both systems are provided in section B in the SI. For **2Co$_2$**, we find that the shortest intermolecular Co(II)···Co(II) distance for the two differently oriented molecules is 9.7976(8) Å; thus, any operative intermolecular interaction should be larger than in **1Co$_2$**.

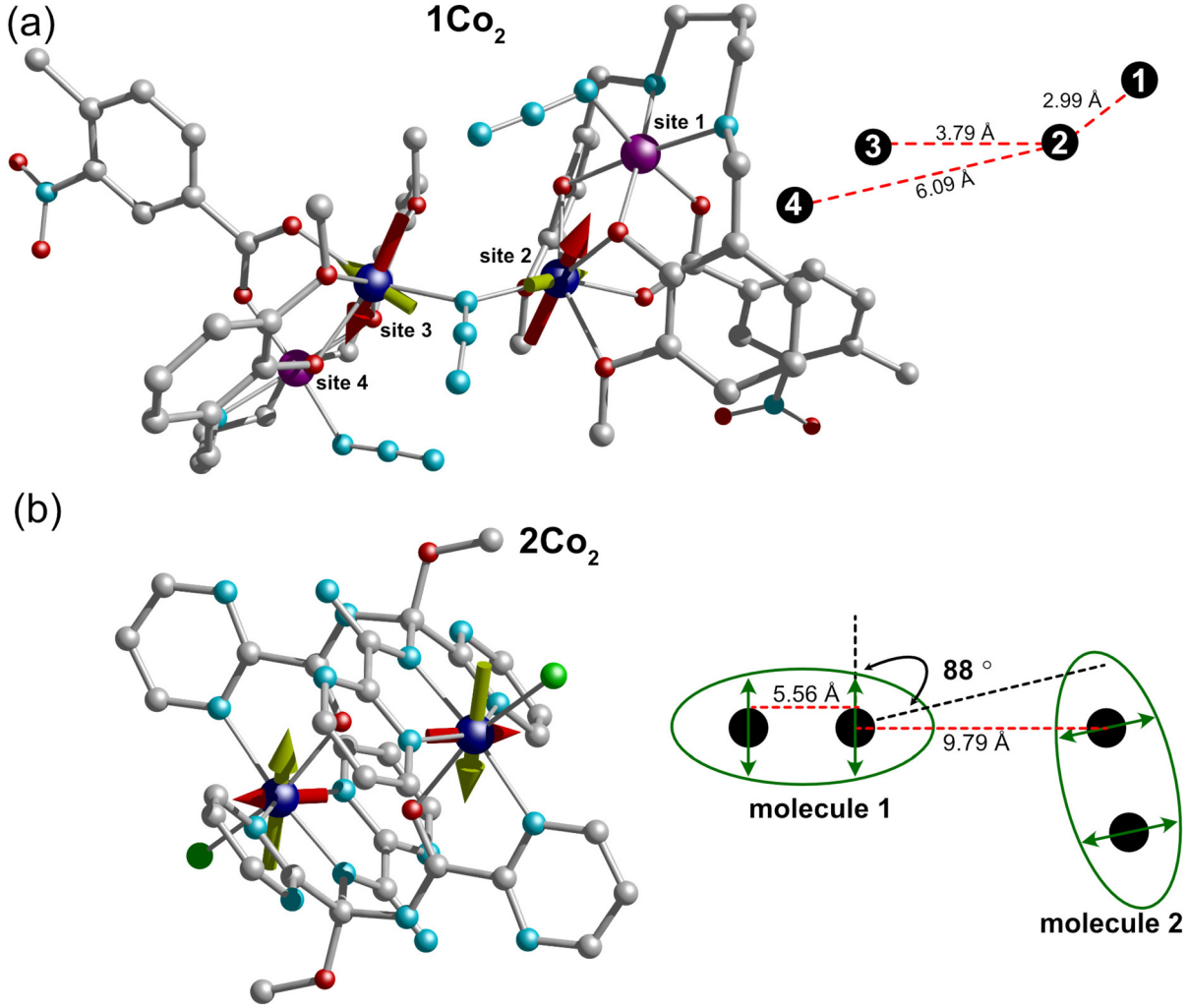

Fig. 1 Crystal structure of Co(II) dimers: (a) Crystal structure for **1Co$_2$** and schematic diagram of Co ions and the intramolecular distances within the complex; (b) crystal structure for **2Co$_2$** and schematic representation of the two differently oriented molecules within the unit cell and the angle between the easy axes. The direction of the easy (green arrows) and hard (red arrows) axes is shown as determined from CASSCF calculations. The longer arrows indicate the dominant anisotropy axis in each case. Colour code: Co(II), blue; Co(III), violet; Cl, green; N, cyan; O, red; C, grey. Hydrogens were omitted for clarity.

Hamiltonian for Co(II) dimers

At a single ion level, the Co(II) ion is characterised by a ground state ^{4}F separated by 10^4 cm^{-1} from the ^{4}P first orbital excited state. The ^{4}F splits into three states in a cubic crystal field, two of which are triplet states ($^4T_{2g}$ and $^4T_{1g}$), and a singlet state ($^4A_{2g}$), with the $^4T_{2g}$ lying lowest. Due to isomorphism, some mixing occurs between the ^{4}P and the ^{4}F($^4T_{1g}$). Moreover, strong first-order spin–orbit coupling between the 12-fold degenerate ground $^4T_{1g}$ state (with S = 3/2 and L = 1) is the norm for Co(II) systems; hence, a Hamiltonian of the form of (1) is suited in such environments.

$$\hat{H}_{SOC} = -\alpha\lambda\hat{\boldsymbol{L}}_{Co}\cdot\hat{\boldsymbol{S}}_{Co} + \Delta_{ax}\left[\hat{L}_{z,Co}{}^2 - \frac{1}{3}L(L+1)\right] + \Delta_{rh}\left[\hat{L}_{x,Co}{}^2 - \hat{L}_{y,Co}{}^2\right] + \mu_B\boldsymbol{B}\cdot\left(-\alpha\hat{\boldsymbol{L}}_{Co} + g_e\hat{\boldsymbol{S}}_{Co}\right) \quad (1)$$

in (1) λ is the Spin–Orbit Coupling (SOC), α is the orbital reduction factor described as $\alpha = A\kappa$, where κ represents the reduction of the orbital momentum by the delocalisation of the unpaired electrons. A represents the contribution of the upper $^4T_{1g}(^4P)$ into the ground $^4T_{1g}(^4F)$ state. Δ_{ax} and Δ_{rh} parameters account for the axial and rhombic distortions of the ideal O_h symmetry of Co(II), which split the $^4T_{1g}(^4P)$ ground manifold. These describe the separation between the singlet $^4A_2$ and doublet ^4E states produced by splitting the $^4T_{1g}(^4P)$ state. A second-order SOC splits $^4A_2$ into two Kramers doublets, while the splitting of the ^4E state renders four Kramers doublets. μ_B and g_e the Bohr magneton and the free electron g-value, respectively.

When considering a dimeric system, an additional parameter must be introduced into (1) to account for the interactions operating between the Co(II) ions, leading to:

$$\hat{H}_{SOC\text{-}dimer} = \hat{H}_{SOC,1} + \hat{H}_{SOC,2} - h\hat{\boldsymbol{S}}_{Co^1}{}^T\boldsymbol{2J}_{ex}\hat{\boldsymbol{S}}_{Co^2} \quad (2)$$

where $\boldsymbol{J}_{ex}$ is an isotropic interaction acting upon the real spins.

By employing eqn (2) it is possible to account for the interactions between the Co(II) ions up to room temperature; however, below 50 K, solely the two lowest doublets are populated (^{4}E). Thus, the zero-field splitting (ZFS) phenomenological method is suited, where $S = 3/2$.[24,36–40,43,44] This allows us to simplify the Hamiltonian by writing it in terms of spin $\hat{\boldsymbol{S}}$ without the requirement of orbital angular momentum $\hat{\boldsymbol{L}}$. For distorted octahedral symmetry of the Co(II) sites, this approach is appropriate. The Hamiltonian is hence:

$$\hat{H}_{\text{S-dimer}} = \sum_{i=1}^{2} \{\mu_B \boldsymbol{B}^T \boldsymbol{g}_i \hat{\boldsymbol{S}}_{i\text{Co}} + hD_i(\hat{S}_{zi,\text{Co}}{}^2 - S(S+1)/3) + hE_i(\hat{S}_{xi,\text{Co}}{}^2 - \hat{S}_{yi,\text{Co}}{}^2)\} h\hat{\boldsymbol{S}}_{\text{Co}^1}{}^T 2\boldsymbol{J}_{ex}\hat{\boldsymbol{S}}_{\text{Co}^2} \quad (3)$$

where D_i, E_i are respectively axial and equatorial anisotropy constants are reduced from the D tensor diagonalised in (x_i, y_i, z_i) frame, *i.e.*, $D_i = 3D_{zi}/2$, $E_i = (D_{xi} - D_{yi})/2$. $\boldsymbol{B}^T$ is the magnetic field vector $(\mu_0 H_x, \mu_0 H_y, \mu_0 H_z)^T$, while $\boldsymbol{g_i}$ are the g-tensors. D is defined based on the largest anisotropy constant along the z-axis and the smallest along the x-axis, *i.e.* $|D_z| > |D_y| > |D_x|$, and $0 \leq E/D < 1/3$.

To deal with such a two-body Hamiltonian, generally, a frame can be chosen that simplifies/diagonalises the interaction tensor $\boldsymbol{J}_{ex}$, while two sets of Euler rotations transform into individual ionic frames (Co_i = 1, 2). Assuming that the g and D tensors are simultaneously diagonalised in the transformed frame for each ion $\{(x_1, y, z), (x_2, y_2, z_2)\}$, the problem involves several independent parameters. Notice that eqn (2) also contains more parameters than (3) when considering single crystal data, and Euler angles between the spins' anisotropy-frames; thus, for both cases, several parameters should be obtained *via* first principles calculations based on crystallographic data as initial guesses.

Sub-Kelvin investigations – μSQUID and μSQUID-EPR

Temperature and sweep-dependent $M(H)$ curves with the field applied along the easy axes were measured employing a μSQUID array and the transverse method[45] (Fig. S9). While the $M(H)$ curves at 30 mK temperature for **1Co$_2$** are completely closed (Fig. S9b), the loops for **2Co$_2$** show mild opening only at high sweeping rates (Fig. S9d). The behaviour indicates fast relaxation in both samples; hence, neither satisfies the conventional definition of single-molecule magnets, that is, neither system possesses a large barrier and/or diminished quantum tunneling rates that would yield slow relaxation of the magnetisation. The small hysteresis observed in **2Co$_2$** might arise from phonon bottleneck effects.[46] Furthermore, any feature in the $M(H)$ curves, which may indicate intramolecular coupling between Co(II) ions, is smeared out above 100 mK temperature (Fig. S9a and c). In conclusion, solely based on the μSQUID results, no further information can be extracted for these systems.

To gain a deeper insight into the physical parameters of **1Co$_2$** and **2Co$_2$**, we utilise the μSQUID-EPR technique, *i.e.* we collect the $M(H)$ data using μSQUID while applying constant frequency (ν) microwave pulses using a co-planar waveguide fabricated on the μSQUID chip (upper inset in Fig. 2a). The resonant microwave absorption produces several sharp peaks, directly observed in the $M(H)$ loops, at the experimental '*resfields*'. The latter is defined as the field magnitudes at which the energy difference between two specified spin states matches the energy of the applied microwave $E(\nu)$. At a fixed ν, the direction of the field (θ) within the SQUID plane is varied with respect to the crystallographic frame to yield the angular maps of the *peaks* ($\Delta M(H,\theta)$); while sweeping over ν at a fixed angle gives the frequency maps ($\Delta M(H,\nu)$) of the *peaks*.

Fig. 2 shows the $M(H)$ curves in **1Co$_2$** and **2Co$_2$**, obtained at 30 mK bath temperature, for a microwave excitation with frequencies ranging between 1–30 GHz. The observed frequency

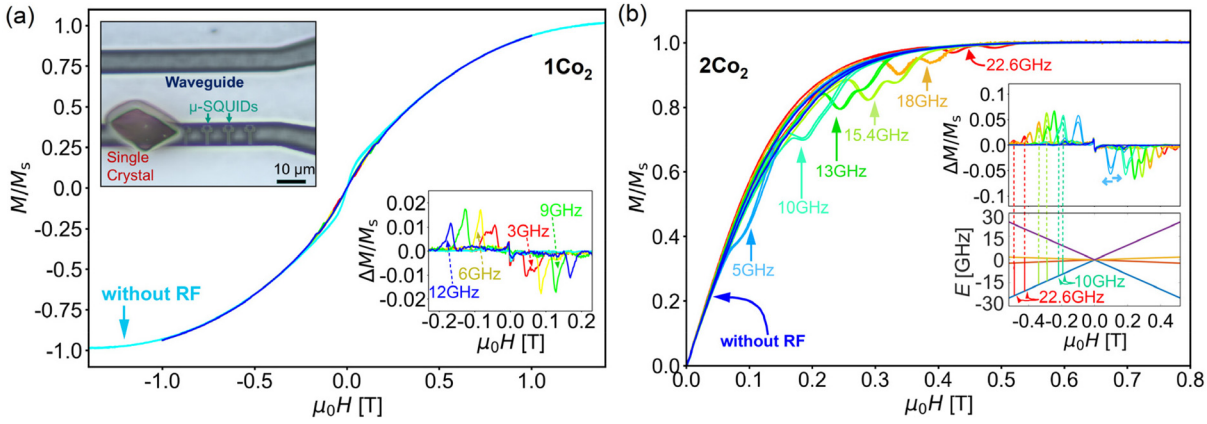

Fig. 2 μSQUID-EPR studies: $M(H)$ curves measured by μSQUID in the presence of microwave excitation with a few fixed frequencies for **1Co$_2$** (a) and **2Co$_2$** (b). The $M(H)$ loops without microwave excitation are also shown in the same panels for comparison. (a) The absorption peaks in **1Co$_2$** are barely visible, but peak subtraction from the baseline curve, renders transitions sufficiently larger than the measurement noise (lower inset). The upper inset shows a μSQUID-EPR chip with a single crystal of a molecular magnet and a coplanar waveguide. (b) For **2Co$_2$** the absorption peaks are large, hence, directly visible in the $M(H)$ loops. The μSQUID-EPR studies were conducted with a power (p), width (w) and delay [$p \sim -6$ dBm, w = 10 μs, d = 300 μs] and different frequencies ranging between 1–30 GHz.

dependence of the peak positions confirms resonant transitions between the spin states of the molecule. For **1Co$_2$**, these absorption peaks are small and barely visible in the $M(H,\nu)$ curves (Fig. 2a). Nevertheless, upon baseline subtraction, the peaks appear sufficiently larger than the measurement noise (Fig. 2a lower inset). For **2Co$_2$**, the peaks are rather large and visible directly in the $M(H,\nu)$ curves shown for the positive fields in Fig. 2b. The inset of Fig. 2b indicates that the observed peaks can be explained by considering resonant transitions between certain states of the Zeeman diagram, simulated for an appropriate angle of the applied field and specific parameters for the given molecule (*vide infra*).

The resonant microwave absorption peaks can be directly mapped into angular and frequency maps by either varying the applied field direction or the microwave frequency, as shown in Fig. 3. Fig. 3a and b show the angle-dependent map of the resonant peaks ($\Delta M(H,\theta)$) at ν = 8 GHz, for **1Co$_2$**. Two intersecting ellipses with nearly the same amplitudes of the long and the short axes are noticeable, providing information about the underlying spin Hamiltonian parameters characterising the system. Fig. 3c shows a frequency-dependent map of the resonant peaks $\Delta M(H,\nu)$ exhibiting linear behaviour. This is obtained for the field applied along the magnetic X-axis as indicated by the white dashed line in Fig. 3a. Furthermore,

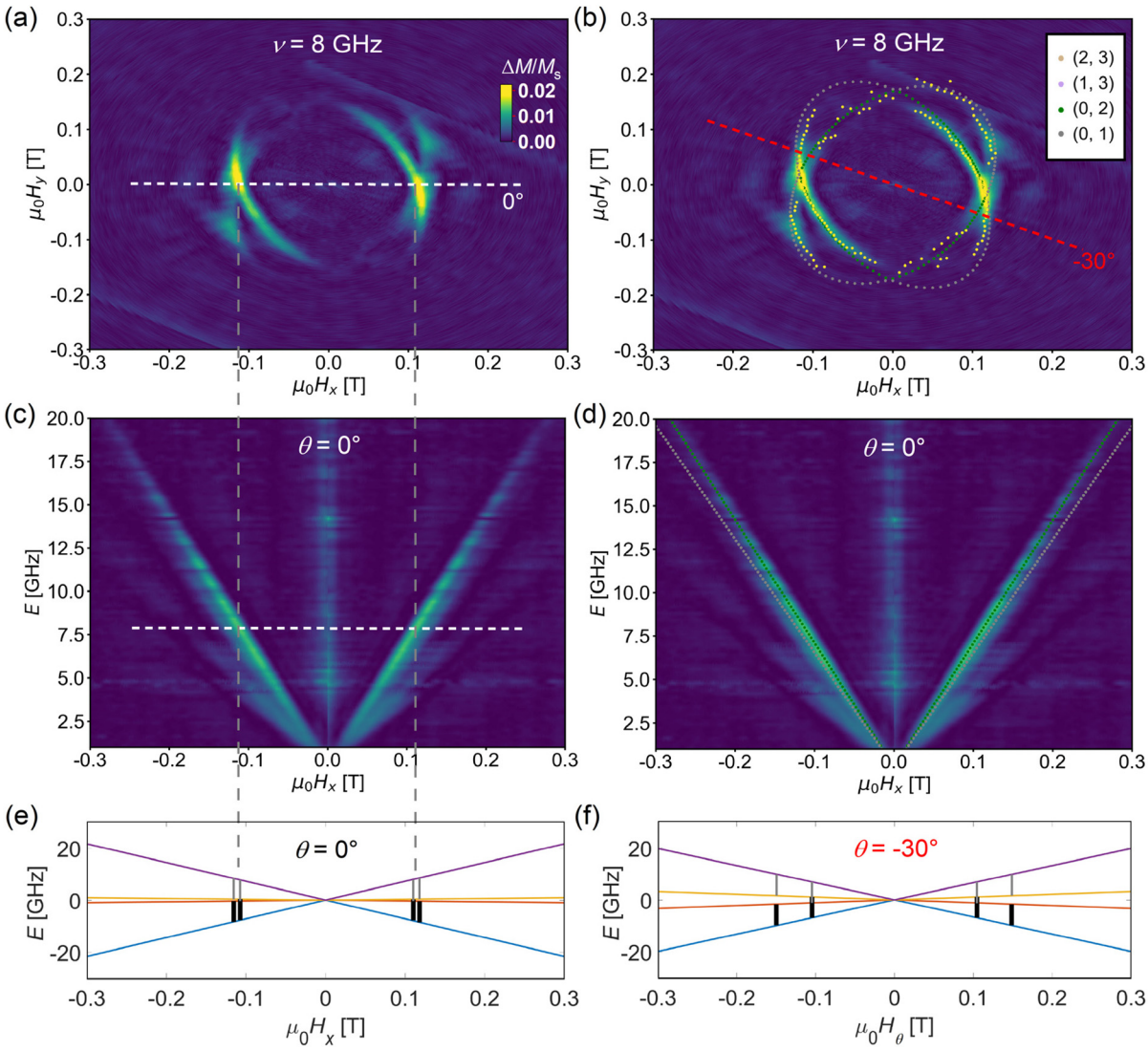

Fig. 3 Angular and frequency μSQUID-EPR for **1Co$_2$**: EPR absorption maps and fits. The angle-dependent absorption map, *i.e.*, $M-M_{base}(H_{x,y})$ for fixed frequency ν = 8 GHz is shown in panel (a). The corresponding fitted map is shown in panel (b) with the yellow dots as the maxima found by the peak-finder from the experimental maps. At the primary stage, the interaction is assumed to be J = 0; hence, the transitions (2,3) and (1,3) superpose with (0,1) and (0,2), respectively. The frequency-dependent absorption map, *i.e.* $M-M_{base}(\nu, H_x)$ and its simulation, for a fixed direction of the applied field, are shown in (c) and (d), respectively. The dashed line in (a) shows the direction of the applied field corresponding to (c), while the dashed lines in (c) show the frequency of the applied microwave corresponding to (a); (e) shows the Zeeman diagram for a 0° angle of the applied field as demonstrated by the white dashed line in (a); (f) Zeeman diagram with a −30° angle as shown by the red dashed line in (b). The *resfields* for ν = 8 GHz excitation (vertical bars) are indicated in each Zeeman diagram.

the angle-dependent map highlights the anisotropy of the system, revealing immediate signatures of two differently oriented spins in the molecule with a tilting angle between the anisotropy axes. Moreover, in the frequency-dependent map, a non-zero intercept of the linear absorption lines to the *X*-axis and any distortion from the linear behaviour can usually be associated with intra-molecular interactions. In contrast, the maps (Fig. 3c) show no clear evidence of distortion or large intercept, indicating nearly no interaction in **1Co$_2$**.

The angular and frequency-dependent maps for **2Co$_2$** are shown in Fig. 4a–c. In contrast to **1Co$_2$**, two ellipses with one almost exterior to the other are observed. Fig. 4d and e show the frequency-dependent maps of the resonant peaks ($\Delta M(H,\nu)$) for **2Co$_2$**, obtained at two different angles as indicated in Fig. 4c. Despite the apparent differences with **1Co$_2$**, the angle-dependent map in **2Co$_2$** also indicates two magnetic cores in the system with their anisotropy axis tilted with respect to each other. The lack of significant variation in the shape of absorption lines in Fig. 4a–c and no obvious distortion from linear behaviour in the frequency maps in Fig. 4d and e suggests that the interactions are likewise negligible.

High temperature regime – SQUID magnetometry

DC magnetic susceptibility data (2–300 K) were collected on restrained powdered samples of **1Co$_2$** and **2Co$_2$** using a SQUID magnetometer, applying a magnetic field of 1 kOe. $M(H)$ were also carried out in the temperature and field range of 2–5 K and 0 to 5 T, respectively. The room temperature $\chi_M T$ value for complex **1Co$_2$** was found to be 5.16 cm^3 mol K^{-1} (Fig. S7), in good agreement with the expected value for two uncoupled Co (II) ions characterised by an $S = 3/2$ spin (*i.e.*, 5.13 cm^3 K mol^{-1} for two Co(II) with $g = 2.59$). Upon cooling, the $\chi_M T$ value

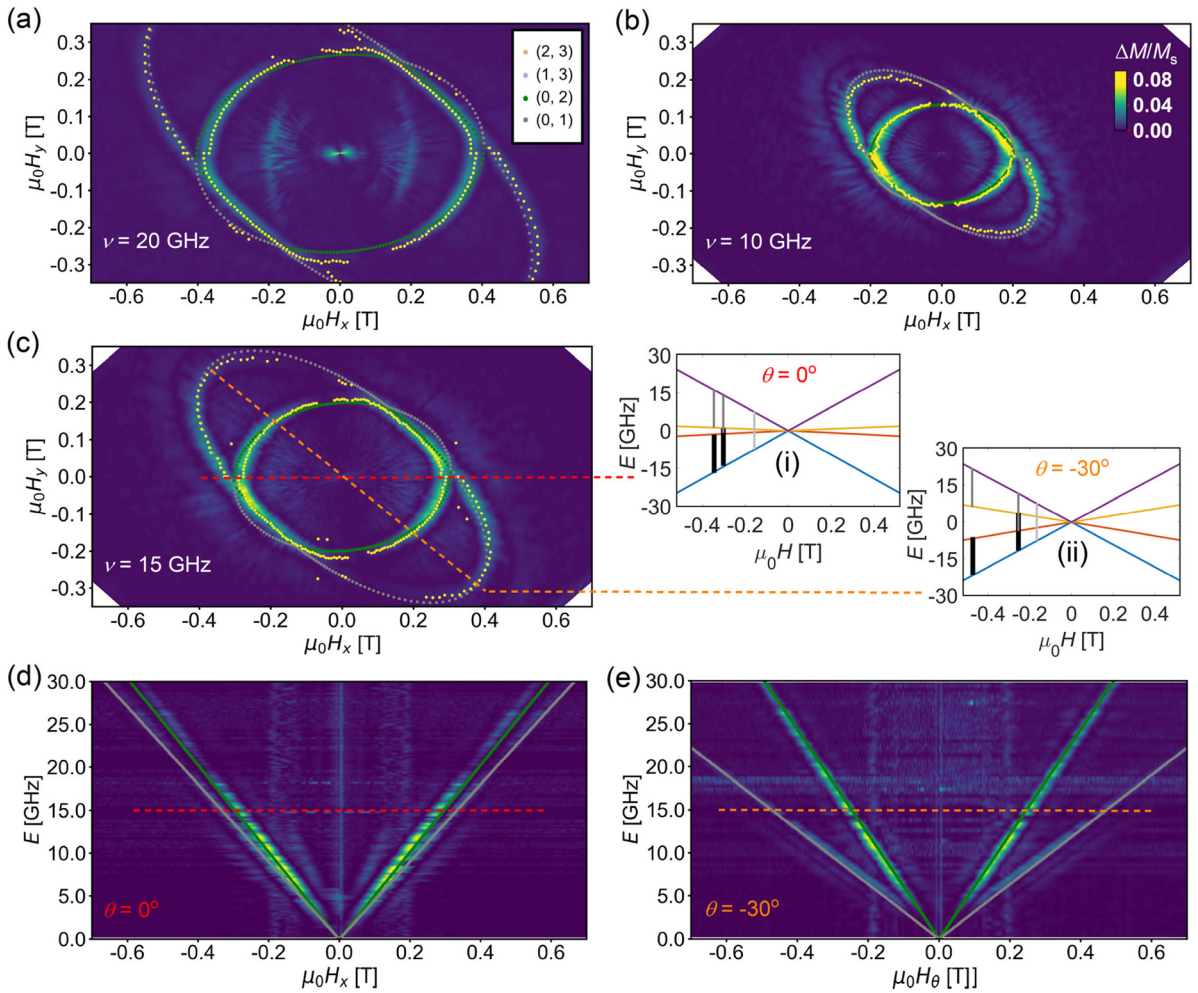

Fig. 4 Angular and frequency μSQUID-EPR for **2Co$_2$**: EPR absorption maps for **2Co$_2$** with its fittings: The angle-dependent absorption maps, *i.e.*, $M-M_{base}(H_{x,y})$ for fixed frequency ν = 20 GHz, 10 GHz and 15 GHz are shown in (a), (b) and (c) respectively. The corresponding fitted lines (grey and green) are also shown with the maxima (yellow dots) found by the peak finder from the experimental maps. The frequency-dependent absorption map, *i.e.* $M-M_{base}(\nu)$, H_x with its simulated curve a for a fixed direction of applied field θ = 0° and 150° are shown in (d) and (e) respectively. The red and orange dashed lines in (c) indicate the direction of the applied field corresponding to (d) and (e). Panels (i), (ii) show the Zeeman diagrams, simulated for these two angles, indicating *resfields* for ν = 15 GHz excitation (vertical bars) to clarify the observed angular dependence in (c).

increases slowly as the temperature is decreased down to ~18 K, where it more rapidly drops down to 2.9 cm^3 mol K^{-1} at 2 K. The upturn signals operative ferromagnetic interactions, while the downturn could be ascribed to the depopulation of excited levels. For **$2Co_2$**, we find that the room temperature $\chi_M T$ value is also close to the expected for two uncoupled Co(II) ions characterised by an $S = 3/2$ spin with a value of 6.1 cm^3 K mol^{-1} (*cf.*, 6.3 cm^3 K mol^{-1} for two Co(II) with $g = 2.59$) (Fig. S8). Upon cooling, the $\chi_M T$ product decreases gradually, reaching a value of 2.3 cm^3 K mol^{-1} at 2 K. The downturn in **$2Co_2$** can be a consequence of the depopulation of anisotropic levels and/or antiferromagnetic interactions. The relatively similar $\chi_M T$ value at 2 K signals a similar low-temperature energy manifold.

Magnetisation studies likewise reveal no saturation of the ground state at 2 K up to 5 T for **$1Co_2$** and **$2Co_2$**, with the highest $M(H)$ value at the lowest temperature and highest field reaching 4.1 and 3.1μ_B, respectively.

Discussion

For a comprehensive understanding of the experimental sub-Kelvin μSQUID-EPR data, it is necessary to visualise the spin Hamiltonian (eqn (3)) in terms of the Zeeman diagram and its variation with the direction of the applied external magnetic field for a hypothetical case (Fig. 5a and b). Fig. 5c and d shows the angular variation of the simulated '*resfields*', for three specific transitions. For this, a hypothetical Co(II) dimer was chosen, each ion characterised by an $S = 3/2$ state and a large D_i and E_i values (with a $D_i/E_i = 1/4$) and isotropic g-values. The simulations were carried out employing Easyspin.[47] For simplicity, at first, we assume no interaction between the ions while simulating Fig. 5. The model, however, considers the possibility of an intra-tilt between the anisotropy axis frames of Co(II) ions. The Euler angles (Fig. 5c and d) for each ion were chosen such that the largest anisotropy axis (in this case, the hard axis) between the two makes a 60° angle, while

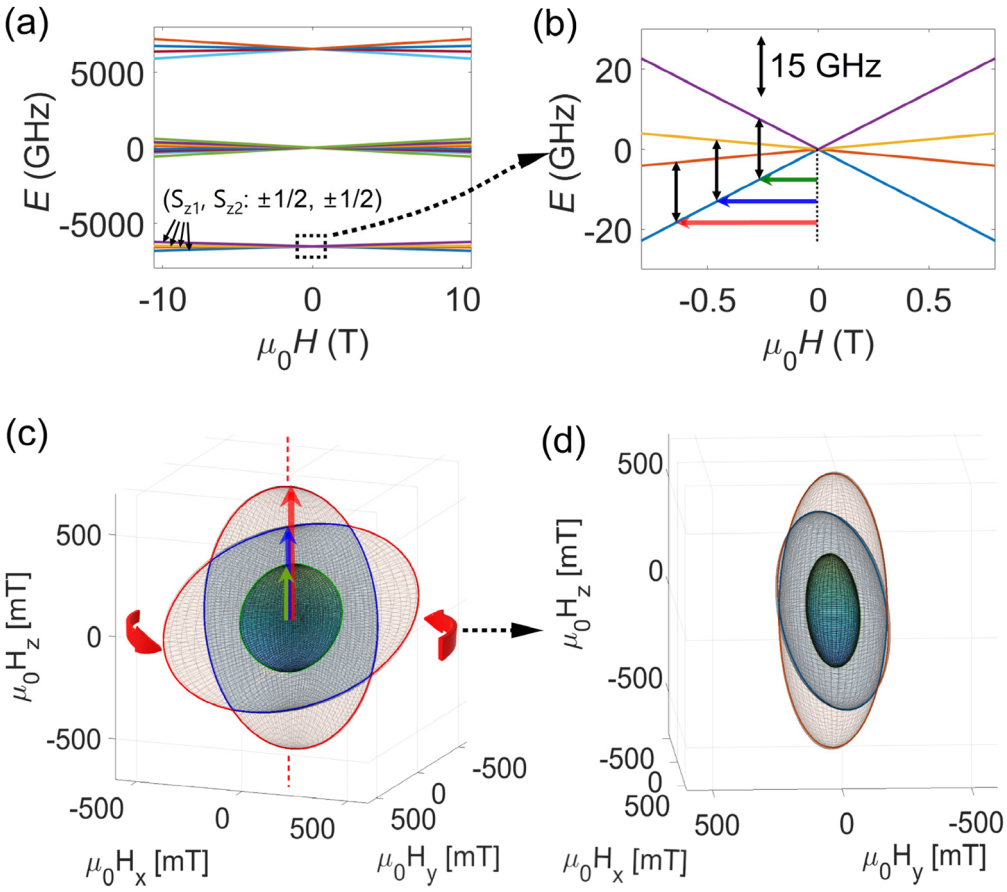

Fig. 5 Angular variation of the resonance field for Co(II) dimer: (a) Zeeman diagram for a hypothetical spin dimer with an angle between their anisotropy axis, modelled using $S_{1,2} = 3/2$ with $D_{1,2} = +100$ cm^{-1}, $E_{1,2} = +25$ cm^{-1}, Euler angles [0 −60 10], [0 0 −10] and $g = 2$. For simplicity the case of zero interaction ($J = 0$) is shown here while the cases for non-zero J with different orders of magnitude are analysed in the SI. At sub-Kelvin temperatures, solely the ground multiplet is expectedly to be populated. (b) Zoomed region of the ground multiplet and the resonance fields for ν = 15 GHz. The red arrow is the *resfield* for the excitation to the first excited state, while the blue and green arrows are the excitation to the second and third excited states. (c and d) Angular dependence of the *resfield* for ν = 15 GHz and comprising excitations to the first, second and third excited states for $S_{1,2} = 3/2$ dimer shown using two projections. The non-colinear arrangements between the spin results in the tilted ellipsoid shapes in the *resfields*.

another 20° rotation in the perpendicular plane (in this case, the easy plane) follows. Due to the large D_i and E_i values, considering only the four lowest states in the ground multiplet is sufficient to describe the system at sub-Kelvin temperatures (*vide supra*). These four states (zoomed region in Fig. 5b) can be rationalised as originating from two states in the ground doublet for a single $S = 3/2$ system. The Zeeman diagram for a fixed direction of field contains only a small representation of the spin Hamiltonian, as it varies drastically with the angle of the applied field. For instance, the magnitude of *resfield* for a 15 GHz quantum of excitation between the ground state to the 1st excited state is shown by the red arrow in Fig. 5b for a specific direction of field. Varying the direction of the field (θ, φ) with respect to the molecular frame for this excitation yields the red surface in panels Fig. 5c and d. Similarly, the angular variation of the *resfields* for 15 GHz between the ground state and 2nd and 3rd excited states (blue and green arrows in Fig. 5b, respectively) is displayed by the blue and greenish surface in Fig. 5c and d. The direction of the field in Fig. 5b is indicated by the arrows in Fig. 5c.

Due to non-colinear arrangements in the hypothetical Co(II) dimer, the angle between the hard axes of the ions results in two tilted ellipsoids in the 3D angular plot of the resonance fields. Note that the largest values of *resfields* indicate the hard axis, and the smallest values are obtained along the easy axis. Fig. 5c shows the anisotropy in such molecular systems consisting of two transition metals with $S = 3/2$. It is worth noting that the magnitude of the *resfield* ellipsoids heavily depends on the g values, while the ellipticity is dictated by E/D ratio. Furthermore, we chose both D and E to be positive, which for small E would have resulted in prolate ellipsoids—indicating a hard axis and easy plane. If both D and E were negative, a small E would instead lead to oblate ellipsoids, signifying a unique easy axis and hard plane. However, when E approaches $D/3$, an easy, hard, and intermediate anisotropy axis becomes prominent. For $E \sim D/3$, a negative D, E and a positive D, E scenario do not differ drastically as the easy and the hard axis closely compete to be the dominant anisotropy axis (see Fig. S10). These different categories are encountered in this study. Experimentally, the angle between two participating spins can be visualised in Fig. 5c and d as an angle between the two ellipsoids. Interestingly, the intersecting ellipsoid *resfield* surfaces may also appear as outer and inner ellipses depending on the plane of 2D projection, see Fig. 5d.

Based on this hypothetical model and the sub-Kelvin μSQUID-EPR experimental data obtained for **1Co$_2$** and **2Co$_2$**, it can be inferred that the magnetic interactions within the dimeric units are minimal or effectively negligible. These findings are in stark contrast to the high-temperature SQUID magnetometry data, where clearly large ferromagnetic and antiferromagnetic interactions are visible. To quantify the interaction observed in high-temperature SQUID data, we employ Hamiltonians (2) and/or (3), leading to a strong ferromagnetic interaction of $J_{ave} \sim 4$ cm^{-1} and ~ -6 cm^{-1} for **1Co$_2$** and **2Co$_2$**, respectively (see SI section C.1 for details).

To resolve this contradiction, we explore the hypothetical dimer model in both the regimes of large and small interactions. Introducing a small interaction between the ions results in the opening of anti-level crossings or mixing of states in the Zeeman diagram, mostly near zero field with small distortions of these *resfield* surfaces. If the interaction is significantly smaller than D, E and a half integer spin is concerned, the exact role of interaction can be clearly distinguished from the effect of transverse parameters E on the frequency scans, as shown in the simulations in Fig. S11 with and without a small interaction. This simulation also highlights the mentioned small distortion of the *resfield* surfaces. On the other hand, when interaction is comparable to the magnitude of D, E, it is often experimentally impossible to distinguish it from the role of E. Nevertheless, we extend the hypothetical model to simulate the case of large interactions and investigate the Zeeman diagram with possible EPR transitions in such a case. When an isotropic large interaction of the order $\sim\pm5$ cm^{-1} (comparable with DC SQUID results) is introduced, the Zeeman diagram has been found to drastically change, giving an effective coupled spin-like scenario with no EPR transitions below <50 GHz microwave frequency (see Fig. S12).

To address this conundrum and to choose a reliable route of analysis, we delve into the structural and anisotropic parameters obtained *via* CASSCF/SO-RASSI/SINGLE_ANISO calculations.[31,48] Crystallographically, **1Co$_2$** possesses one molecular orientation in the unit cell (two molecules related by inversion symmetry), while **2Co$_2$** involves two molecular orientations at a large angle (Fig. S5, S6 and S13). The case of **1Co$_2$** turned out to be quite convoluted. As there is no angle between two neighbouring molecules' spins, the two observed angles cannot be explained by intermolecular orientations. We also noticed that the μSQUID-EPR peaks were very weak compared to **2Co$_2$**. This points to the possibilities involving impurity/defect molecules in the lattice. For **1Co$_2$**, four Co sites with two non-magnetic Co(III) at the periphery and two Co(II) near the centre of the molecule are observed. In this scenario, with two neighbouring Co(II) ions, strongly interacting, our hypothetical model with large coupling (Fig. S12) would render no EPR transition (below < 50 GHz) as well. However, considering the charge balance intact within the molecule, the most plausible impurity/defect scenario is a swapping of ions between a Co(II) and a Co(III) sites. A model involving Co(II) ($S = 3/2$) only at 2nd and 4th site (and parallelly Co(II) only at 1st and 3rd site, see Fig. S13 and schematic in Fig. 1a) seemed most convincing to explain the μSQUID-EPR peaks (Fig. 3), especially after noticing that the CASSCF simulations for such a model yields angles that very well match with that obtained from the μSQUID-EPR angular maps on **1Co$_2$** (*vide infra*). This would mean that a small fraction of molecules exhibits a very weakly interacting $S = 3/2$ dimer (at 2nd and 4th site, or 1st and 3rd site), accounting for the μSQUID-EPR maps. While the majority of **1Co$_2$** molecules (strong interaction) with Co(II) at 2nd and 3rd site account for the observed in DC SQUID data.

The impurity in **1Co$_2$** was modelled employing eqn (3) by considering the Co(II) to be located at 2nd and 4th sites, with the input of CASSCF at these locations. However, as the ligands at these two sites are not identical, the CASSCF yields very different anisotropic parameters between these two sites. We obtain D_1 = 33.03 cm^{-1}, E_1 = 5.51 cm^{-1} for 'site 2' and D_2 = −71.04 cm^{-1}, E_2 = −21.42 cm^{-1} for 'site 4'. The Euler angles for the largest anisotropy axis (for 2nd and 4th sites), as obtained by CASSCF simulations (Fig. S13 and Table S8) were Co^1 ≈ [−41 49 60]° and Co^2 ≈ [70 42 131]°. Using fixed $D_{1,2}$, $E_{1,2}$ and these angles as initial values, we finally fit the μSQUID-EPR maps as shown in Fig. 3b and d. The fitting yields $\boldsymbol{g_1}$ = [2.54, 2.63, 2.40], $\boldsymbol{g_2}$ = [3.43, 2.27, 2.24] (with Δg_{max} = 0.07); Euler angles (with respect to the lab frame $H_{x,y,z}$) for Co^1 = [−41.6 49.4 59.5]° and the Euler angles for Co^2 = [64.0 41.8 130.7]° (with $\Delta\theta_{max}$ = 1°). The excellent matching with the CASSCF obtained angles clearly indicates that the measurement plane was very closely related to the 'a–c' crystallographic plane (see Fig. S13: crystallographic plane projected on the μSQUID plane). The case for Co(II) at 1st and 3rd sites was also analysed (Fig. S15) and found to complete the observed features in the angular maps in Fig. 3. In addition, a small intermetallic interaction (as expected assuming only dipolar contribution between next nearest sites) is estimated as the dominant contributor to the broadening of the peaks (see section G.2 in SI). The estimated interaction between the Co(II) placed at 2nd and 4th sites: J ∼ 0.003 cm^{-1} was of the same order of magnitude compared to purely dipolar interaction ∼0.007 cm^{-1}, considering the distance and tilt between 2nd and 4th sites (Table S9).[49] The two ellipses visible in Fig. 3a and b have nearly similar major and minor axes, indicating that both the hard axes of the two Co(II) ions in **1Co$_2$** lie symmetrically close to the measurement plane, a situation comparable to the line cuts of the surfaces shown in Fig. 5c. On the other hand, the frequency map in Fig. 3c and d displays a linear behaviour indicative of the Zeeman splitting, with a major contribution from (0,1); however, the *resfield*s for the transition (0,2) also lie very close at this angle (grey and green lines in Fig. 3d). Some additional features, which were very weakly visible in the frequency maps in Fig. 3c, could be explained as well, as the case for Co(II) at 1st and 3rd sites was also included (see Fig. S15). The weak EPR signal in **1Co$_2$** leads to a large margin of error in this analysis; however, it points to the impurities, which are only a small fraction of the molecules. X-band EPR and μSQUID-EPR intensity analysis (phenomenological) both hint at ∼1.8% impurity present in **1Co$_2$**, supporting our model (see sections I, J in SI for details). Although studies of the impurity-free compound would be ideal, the fact that the Co(III) sites are formed *in situ* during the reaction conditions precludes the synthesis of such systems.

For **2Co$_2$**, however, a different scenario is found: a large μSQUID-EPR signal (and large X-band EPR intensity compared to **1Co$_2$**, see section J in SI) in this sample rules out the possibilities that involve modelling with an impurity molecule. We further notice that for **2Co$_2$** CASSCF calculations yield parallel anisotropy axes between the two Co(II) within a molecule, but two directions within the packing (schematic in Fig. 1b and Fig. S13), hence confirming that the visible two orientations in the μSQUID-EPR angular maps (Fig. 4) are due to the intermolecular (packing) angle. Due to the parallel anisotropy axis and large interaction within a molecule as predicted by SQUID measurements, each molecule could be represented by an effective spin. The non-isotropic nature and the magnitude of the interaction (not infinitely large, but comparable to D, E) prohibit an exact total spin representation. We also found that such effective spin (one per molecule) model with appropriate parameters can mimic the low-lying states of the more general model, *i.e.* a 4-spin Hamiltonian (strong intra and weak inter molecular coupling) considering two molecules at an angle. Hence, in the upcoming discussion, we model **2Co$_2$** as an effective spin S = 3/2 dimer exhibiting intermolecular angles and small intermolecular interactions (also see section G.2 in SI).

For the **2Co$_2$**, the $\Delta M(H,\theta)$ maps (Fig. 4a–c) show two ellipses with different ellipticities, one appearing almost like a circle. Based on the angular and frequency maps, the intermolecular interactions can be ignored for the primary stage of analysis. Furthermore, the two ellipses with different ellipticities shown in Fig. 4a–d indicate that the measurement plane is not symmetric concerning the two molecular orientations. This situation can be compared to the line cuts of the surfaces in the theoretical model in Fig. 5d. Fitting the angular maps and the frequency maps leads to the final set of parameters for this system as: $D_{1,2}$ = −68.64 cm^{-1}, $E_{1,2}$ = −21.52 cm^{-1}, $\boldsymbol{g_1}$ = [3.75, 3.01, 2.35], $\boldsymbol{g_2}$ = [3.73, 3.14, 2.50], (with Δg_{max} = 0.08); Euler angles (with respect to the lab frame $H_{x,y,z}$) for the two orientations of molecules = [48, 53, −25], [91, −58, 9] (with $\Delta\theta_{max}$ = 1°) leading to an angle between the two easy axis ∼100°. The obtained value is close to that calculated from CASSCF for the molecules residing in the unit cell (∼88°). In this case, it is not possible to unambiguously determine the measurement plane of the crystal. Similarly to **1Co$_2$**, a weak intramolecular Co–Co interaction is necessary to describe the weakly visible lines in the absorption maps (Fig. S16e and f). The estimated intermolecular interaction J ∼ 0.02 cm^{-1} (anisotropic $\boldsymbol{J}$ = [0.020, −0.015, −0.005]) was larger than the purely dipolar interaction with the order of magnitude ∼0.004 cm^{-1} considering the intermolecular distances and tilt (Table S9).[49] This possibly indicates that the orientation of pyrazine part in the ligands allows a mild π–π intermolecular exchange interaction (see Fig. S6).

Since both systems are eventually modelled with two weakly interacting spin 3/2, the possible EPR transitions can be commonly marked by comparing with the hypothetical case in Fig. 5(b) associated with eqn (3). In this Zeeman diagram, six transitions are expected for a constant frequency of excitation: one occurring between the zero and 3th state (0,3) (green arrow in Fig. 5b), a second transition between the zero and 2nd state (0,2) (blue arrow in Fig. 5b), a third transition between the zero and 1st (0,1) (red arrow in Fig. 5b). Due to the symmetry of the Zeeman diagram and the absence of intermolecular interaction, two other transitions occur at the same field, *i.e.*, a transition between the 1st and 3rd state (1,3) and a transition between the 2nd and 3rd state (2,3), with the same resonance

field as transitions (0,3) and (0,2), respectively. A 6th transition would also be expected between the 1st and 2nd states (1,2); however, it would occur in a much larger field than our experimentally accessible conditions. At our working temperature, it is safe to conclude that the strongest peaks would be associated only with (0,1) and (0,2), corresponding to transitions from the ground state.

Once the fitting parameters from the angular and frequency maps for both complexes are obtained, the exact Zeeman diagrams for two specific angles could finally be simulated. Fig. 3e, f and 4c (panels) show the Zeeman diagram for two appropriate angles with respect to the crystal, which represents the two directions in the measurement plane (0° and −30° with respect to the magnet H_x axis) indicated by white and red dashed lines (Fig. 3) and red and orange dashed lines (Fig. 4). In these diagrams, a vertical bar is fitted to the gap between any two states in resonance with the microwave energy (shown only for the negative fields in Fig. 4c). The results show that the experimental peaks are exactly at the *resfields* for transitions (0,1) and (0,2) and explain the angular evolution of the observed peak positions.

It is worth noting that despite the qualitative similarities in the experimental results and theoretical modelling between **1Co$_2$** and **2Co$_2$**, the origin of the two weakly interacting spins (oriented at an angle) in these two systems is very different. The results in **1Co$_2$** highlight that a strongly coupled system, which is usually EPR silent, can exhibit some weak resonant absorptions in the presence of impurities involving magnetic ions at larger distances. It also signifies that weakly coupled systems are interesting for their multiple states addressable within the usual microwave frequency range.[50] On the other hand, the results in **2Co$_2$** showcase the role of intermolecular tilt angles and interactions on the addressable quantum states in single-crystalline molecular systems, and the capability of the angle and frequency resolved μSQUID-EPR technique to identify these details.

An alternative approach to describe the system is by an effective spin dimer (S_{eff}: 1/2, 1/2) with anisotropic g values compensating the effects of D, E anisotropies to the ground multiplet. This approach leads to a nearly similar quality of fitting; however, it is a simplified view of these systems and does not provide complete information about the spin Hamiltonian (see SI, Fig. S17). Due to the limited accessibility to exact D, E values with our present μSQUID-EPR scheme, the use of the CASSCF results drastically enhances the fitting reliability and decreases the fitting times. Despite these limitations, finally we show that our models are reliable at least within the scope of low frequency EPR by measuring conventional X-band EPR spectrum on the powder sample of each system (Fig. S20) and simulating these with the same parameters used on corresponding μSQUID-EPR maps. Note that the access to these parameters, with fine details such as intermetallic and intermolecular angles, and pinpointing the type of crystal impurity discussed in this study, is commonly difficult, and the number of parameters often precludes the correct and comprehensive understanding of multi-spin systems.

Conclusion

In this study, two Co(II)-based dimeric spin systems were thoroughly characterised by reconciling conventional magnetic measurements down to T = 2 K with frequency- and angle-resolved μSQUID-EPR spectroscopy conducted at 30 mK. Initially, a stark contrast was found between conventional SQUID data exhibiting strong interactions in the dimer and μSQUID-EPR maps suggesting weak interactions. The contradiction was resolved by investigating the μSQUID-EPR maps with inputs from CASSCF calculations, to find that the weak interaction was associated with spin components at large distances with a tilt between their anisotropy axis, coexisting with the strongly coupled Co(II) dimers. To resolve the puzzle of contrasting results, the Zeeman diagrams for hypothetical spin dimers, encompassing different regimes of interaction, were investigated. This offered a broad theoretical perspective on multi-spin systems and emphasised how weak coupling yields multiple spin states addressable with conventional microwave frequency ranges (see Fig. S18). This behaviour differs in strongly coupled systems, where the large energy separation between molecular states limits accessibility. As a result, when dipolar interactions are weak, new states become available for selective manipulation.[50]

A critical takeaway from this study is that when intermetallic (or intermolecular) coupling is weak and the anisotropy axes are tilted relative to one another, simultaneous diagonalisation of the spin Hamiltonian or the use of effective total spin approaches becomes infeasible. Hence, while analysing EPR transitions on such a single molecular crystal, it is important to consider inter-molecular tilt angles among the participating spins, as well as possible impurities, as these can even dominate the observed peaks.[50] Notably, our μSQUID-EPR maps demonstrate the capability to resolve inter-molecular tilt angles and interactions as subtle as 0.01 cm^{-1}, as shown in **2Co$_2$** It is worth noticing that the SQUID and μSQUID-EPR techniques appear not as conflicting but rather as complementary, *i.e.*, during the fitting of SQUID data, the weak interactions can be assumed negligible in comparison to the strong interactions; conversely, strong interactions exceed the measurement limits of μSQUID-EPR techniques. Hence our approach exemplifies how the integration of magnetisation and spectroscopic measurement techniques can transcend the limitations of individual methods, prevent misinterpretation and provide a comprehensive view of complex molecular spin systems.

Author contributions

The idea was conceived by S. P., S. C., M. D., and W. W. The project was supervised by W. W. R. S. S., S. C., J. N. G. and M. D. synthesised the samples. G. N. and E. M.-P. carried out the DC SQUID data collection, analysis and processing. S. P., A. S. and W. W. carried out the μSQUID and μSQUID-EPR data collection. B. B., F. E. and M. G. B. D. carried out crystallo-

graphic studies, data reduction and refinement. E. M.-P. carried out the CASSCF calculations and interpretation. The data was analysed and interpreted by S. P. and E. M.-P. with input from all co-authors. The manuscript was written by S. P. and E. M.-P. with input from all co-authors.

Conflicts of interest

The authors declare no conflict of interest.

Data availability

All the magnetic data was processed employing Origin Pro 2023. The μSQUID-EPR data was all processed using an in-house built software based on Python. The simulation of the μSQUID-EPR was carried out employing an in-house code which works in conjunction with Easyspin implemented in MATLAB.[47]

The data supporting this article has been included as part of the SI: cif files, further synthetic details, structural and magnetic plots. See DOI: **https://doi.org/10.1039/d5qi01387a**.

CCDC 2387470 and 2388164 contain the supplementary crystallographic data for this paper.[51a,b]

Acknowledgements

We acknowledge the DFG-CCR 1573 "4f for future" (project B4) and the Karlsruhe Nano Micro Facility (KNMF, **https://www.kit.edu/knmf**) for the provision of access to instruments at their laboratories. E. M.-P. thanks the Alexander von Humboldt Fellowship for experienced researchers for support. W. W. thanks the German Research Foundation (DFG) for the Gottfried Wilhelm Leibniz-Award, ZVN-2020_WE 4458-5. The authors are grateful to Dr. Alexey Alfonsov, IFW Dresden, and Prof. Rüdiger Klingeler, Heidelberg University, for X-band EPR measurements and discussion.

References

1 E. Coronado, Molecular magnetism: from chemical design to spin control in molecules, materials and devices, *Nat. Rev. Mater.*, 2020, **5**, 87–104.
2 F. Troiani and M. Affronte, Molecular spins for quantum information technologies, *Chem. Soc. Rev.*, 2011, **40**, 3119–3129.
3 E. Moreno-Pineda, C. Godfrin, F. Balestro, W. Wernsdorfer and M. Ruben, Molecular spin qudits for quantum algorithms, *Chem. Soc. Rev.*, 2018, **47**, 501–513.
4 A. Gaita-Ariño, F. Luis, S. Hill and E. Coronado, Molecular spins for quantum computation, *Nat. Chem.*, 2019, **11**, 301–309.
5 N. F. Chilton, Design criteria for high-temperature single-molecule magnets, *Inorg. Chem.*, 2015, **54**, 2097–2099.
6 K. X. Yu, J. G. C. Kragskow, Y. S. Ding, Y. Q. Zhai, D. Reta, N. F. Chilton and Y. Z. Zheng, Enhancing Magnetic Hysteresis in Single-Molecule Magnets by Ligand Functionalization, *Chem*, 2020, **6**, 1777–1793.
7 C. J. Yu, S. Von Kugelgen, D. W. Laorenza and D. E. Freedman, A Molecular Approach to Quantum Sensing, *ACS Cent. Sci.*, 2021, **7**, 712–723.
8 F. Troiani, A. Ghirri, M. G. A. Paris, C. Bonizzoni and M. Affronte, Towards quantum sensing with molecular spins, *J. Magn. Magn. Mater.*, 2019, **491**, 165534.
9 F. S. Guo, B. M. Day, Y. C. Chen, M. L. Tong, A. Mansikkamäki and R. A. Layfield, Magnetic hysteresis up to 80 kelvin in a dysprosium metallocene single-molecule magnet, *Science*, 2018, **362**, 1400–1403.
10 M. Affronte, I. Casson, M. Evangelisti, A. Candini, S. Carretta, C. A. Muryn, S. J. Teat, G. A. Timco, W. Wernsdorfer and R. E. P. Winpenny, Linking rings through diamines and clusters: Exploring synthetic methods for making magnetic quantum gates, *Angew. Chem., Int. Ed.*, 2005, **44**, 6496–6500.
11 J. Ferrando-Soria, E. Moreno-Pineda, A. Chiesa, A. Fernandez, S. A. Magee, S. Carretta, P. Santini, I. J. Vitorica-Yrezabal, F. Tuna, G. A. Timco, E. J. L. McInnes and R. E. P. Winpenny, A modular design of molecular qubits to implement universal quantum gates, *Nat. Commun.*, 2016, **7**, 11377.
12 D. Aguilà, L. A. Barrios, V. Velasco, O. Roubeau, A. Repollés, P. J. Alonso, J. Sesé, S. J. Teat, F. Luis and G. Aromí, Heterodimetallic [LnLn'] lanthanide complexes: Toward a chemical design of two-qubit molecular spin quantum gates, *J. Am. Chem. Soc.*, 2014, **136**, 14215–14222.
13 A. Chiesa, E. Macaluso, F. Petiziol, S. Wimberger, P. Santini and S. Carretta, Molecular Nanomagnets as Qubits with Embedded Quantum-Error Correction, *J. Phys. Chem. Lett.*, 2020, **11**, 8610–8615.
14 S. J. Lockyer, A. Chiesa, G. A. Timco, E. J. L. McInnes, T. S. Bennett, I. J. Vitorica-Yrezebal, S. Carretta and R. E. P. Winpenny, Targeting molecular quantum memory with embedded error correction, *Chem. Sci.*, 2021, **12**, 9104–9113.
15 S. Giménez-Santamarina, S. Cardona-Serra, J. M. Clemente-Juan, A. Gaita-Ariño and E. Coronado, Exploiting clock transitions for the chemical design of resilient molecular spin qubits, *Chem. Sci.*, 2020, **11**, 10718–10728.
16 K. Kundu, J. Chen, S. Hoffman, J. Marbey, D. Komijani, Y. Duan, A. Gaita-Ariño, J. Stanton, X. Zhang, H. Cheng and S. Hill, Electron-nuclear decoupling at a spin clock transition, *Commun. Phys.*, 2023, **6**, 38.
17 M. Shiddiq, D. Komijani, Y. Duan, A. Gaita-Ariño, E. Coronado and S. Hill, Enhancing coherence in molecular spin qubits via atomic clock transitions, *Nature*, 2016, **531**, 348–351.
18 C. Godfrin, A. Ferhat, R. Ballou, S. Klyatskaya, M. Ruben, W. Wernsdorfer and F. Balestro, Operating Quantum States in Single Magnetic Molecules: Implementation of Grover's Quantum Algorithm, *Phys. Rev. Lett.*, 2017, **119**, 187702.

19 M. N. Leuenberger and D. Loss, Quantum computing in molecular magnets, *Nature*, 2001, **410**, 789–793.
20 S. Chicco, G. Allodi, A. Chiesa, E. Garlatti, C. D. Buch, P. Santini, R. De Renzi, S. Piligkos and S. Carretta, Proof-of-Concept Quantum Simulator Based on Molecular Spin Qudits, *J. Am. Chem. Soc.*, 2024, **146**, 1053–1061.
21 A. Chiesa, F. Petiziol, E. MacAluso, S. Wimberger, P. Santini and S. Carretta, Embedded quantum-error correction and controlled-phase gate for molecular spin qubits, *AIP Adv.*, 2021, **11**, 025134.
22 Y.-S. Ding, K.-X. Yu, D. Reta, F. Ortu, R. E. P. Winpenny, Y.-Z. Zheng and N. F. Chilton, Field- and temperature-dependent quantum tunnelling of the magnetisation in a large barrier single-molecule magnet, *Nat. Commun.*, 2018, **9**, 3134.
23 R. Marx, F. Moro, M. Dörfel, L. Ungur, M. Waters, S. D. Jiang, M. Orlita, J. Taylor, W. Frey, L. F. Chibotaru and J. Van Slageren, Spectroscopic determination of crystal field splittings in lanthanide double deckers, *Chem. Sci.*, 2014, **5**, 3287–3293.
24 A. B. Boeer, A. L. Barra, L. F. Chibotaru, D. Collison, E. J. L. McInnes, R. A. Mole, G. G. Simeoni, G. A. Timco, L. Ungur, T. Unruh and R. E. P. Winpenny, A spectroscopic investigation of magnetic exchange between highly anisotropic spin centers, *Angew. Chem., Int. Ed.*, 2011, **50**, 4007–4011.
25 M. J. Giansiracusa, E. Moreno-Pineda, R. Hussain, R. Marx, M. Martínez Prada, P. Neugebauer, S. Al-Badran, D. Collison, F. Tuna, J. Van Slageren, S. Carretta, T. Guidi, E. J. L. McInnes, R. E. P. Winpenny and N. F. Chilton, Measurement of Magnetic Exchange in Asymmetric Lanthanide Dimetallics: Toward a Transferable Theoretical Framework, *J. Am. Chem. Soc.*, 2018, **140**, 2504–2513.
26 E. Moreno-Pineda, N. F. Chilton, R. Marx, M. Dörfel, D. O. Sells, P. Neugebauer, S. Da Jiang, D. Collison, J. Van Slageren, E. J. L. McInnes and R. E. P. Winpenny, Direct measurement of dysprosium(III)···dysprosium(III) interactions in a single-molecule magnet, *Nat. Commun.*, 2014, **5**, 5243.
27 M. Dörfel, M. Kern, H. Bamberger, P. Neugebauer, K. Bader, R. Marx, A. Cornia, T. Mitra, A. Müller, M. Dressel, L. Bogani and J. van Slageren, Torque-Detected Electron Spin Resonance as a Tool to Investigate Magnetic Anisotropy in Molecular Nanomagnets, *Magnetochemistry*, 2016, **2**, 25.
28 J. G. C. Kragskow, J. Marbey, C. D. Buch, J. Nehrkorn, M. Ozerov, S. Piligkos, S. Hill and N. F. Chilton, Analysis of vibronic coupling in a 4f molecular magnet with FIRMS, *Nat. Commun.*, 2022, **13**, 825.
29 M. Perfetti, G. Cucinotta, M. E. Boulon, F. ElHallak, S. Gao and R. Sessoli, Angular-Resolved Magnetometry beyond Triclinic Crystals Part II: Torque Magnetometry of Cp*ErCOT Single-Molecule Magnets, *Chem. – Eur. J.*, 2014, **20**, 14051–14056.
30 E. Moreno-Pineda and W. Wernsdorfer, Measuring molecular magnets for quantum technologies, *Nat. Rev. Phys.*, 2021, **3**, 645–659.
31 L. F. Chibotaru and L. Ungur, Ab initio calculation of anisotropic magnetic properties of complexes. I. Unique definition of pseudospin Hamiltonians and their derivation, *J. Chem. Phys.*, 2012, **137**, 064112.
32 L. Birnoschi and N. F. Chilton, Hyperion: A New Computational Tool for Relativistic Ab Initio Hyperfine Coupling, *J. Chem. Theory Comput.*, 2022, **18**, 4719–4732.
33 A. Lunghi, Toward exact predictions of spin-phonon relaxation times: An ab initio implementation of open quantum systems theory, *Sci. Adv.*, 2022, **8**, 7880.
34 J. G. C. Kragskow, A. Mattioni, J. K. Staab, D. Reta, J. M. Skelton and N. F. Chilton, Spin-phonon coupling and magnetic relaxation in single-molecule magnets, *Chem. Soc. Rev.*, 2023, **52**, 4567–4585.
35 G. Taran, E. Moreno-Pineda, M. Schulze, E. Bonet, M. Ruben and W. Wernsdorfer, Direct determination of high-order transverse ligand field parameters via μSQUID-EPR in a Et4N[160GdPc2] SMM, *Nat. Commun.*, 2023, **14**, 3361.
36 F. Lloret, M. Julve, J. Cano, R. Ruiz-García and E. Pardo, Magnetic properties of six-coordinated high-spin cobalt(II) complexes: Theoretical background and its application, *Inorg. Chim. Acta*, 2008, **361**, 3432–3445.
37 M. E. Lines, Orbital angular momentum in the theory of paramagnetic clusters, *J. Chem. Phys.*, 1971, **55**, 2977–2984.
38 A. V. Palii, B. S. Tsukerblat, E. Coronado, J. M. Clemente-Juan and J. J. Borrás-Almenar, in *Polyhedron*, Elsevier Ltd, 2003, vol. 22, pp. 2537–2544.
39 A. V. Palii, B. S. Tsukerblat, E. Coronado, J. M. Clemente-Juan and J. J. Borrés-Almenar, Microscopic approach to the pseudo-spin-1/2 Hamiltonian for Kramers doublets in exchange coupled Co(II) pairs, *Inorg. Chem.*, 2003, **42**, 2455–2458.
40 S. M. Ostrovsky, K. Falk, J. Pelikan, D. A. Brown, Z. Tomkowicz and W. Haase, Orbital angular momentum contribution to the magneto-optical behavior of a binuclear cobalt(II) complex, *Inorg. Chem.*, 2006, **45**, 688–694.
41 M. Aryaeifar, H. A. Rudbari, E. Moreno-Pineda, J. V. Cuevas-Vicario, S. Paul, M. Schulze, W. Wernsdorfer, F. Lloret, N. Moini and O. Blacque, Synthesis, characterization and magnetic properties of halogenated tetranuclear cubane-like nickel(ii) complexes, *New J. Chem.*, 2024, **48**, 3603–3613.
42 A. Panja, A. Panja, N. C. Jana, S. Paul, W. Wernsdorfer, E. Moreno-Pineda, E. Moreno-Pineda, R. Herchel, P. Brandão, G. Novitchi and W. Wernsdorfer, Insight into ferromagnetic interactions in CuII-LnIII dimers with a compartmental ligand, *Dalton Trans.*, 2023, **53**, 2501–2511.
43 A. V. Palii, B. S. Tsukerblat, E. Coronado, J. M. Clemente-Juan and J. J. Borrás-Almenar, Orbitally dependent magnetic coupling between cobalt(II) ions: The problem of the magnetic anisotropy, *J. Chem. Phys.*, 2003, **118**, 5566–5581.
44 S. M. Ostrovsky, R. Werner, D. A. Brown and W. Haase, Magnetic properties of dinuclear cobalt complexes, *Chem. Phys. Lett.*, 2002, **353**, 290–294.

45 W. Wernsdorfer, N. E. Chakov and G. Christou, Determination of the magnetic anisotropy axes of single-molecule magnets, *Phys. Rev. B: Condens. Matter Mater. Phys.*, 2004, **70**, 132413.
46 I. Chiorescu, W. Wernsdorfer, A. Müller, H. Bögge and B. Barbara, in *Butterfly Hysteresis Loop and Dissipative Spin Reversal in the S 5 1 2, V 15 Molecular Complex*, 2000.
47 S. Stoll and A. Schweiger, EasySpin, a comprehensive software package for spectral simulation and analysis in EPR, *J. Magn. Reson.*, 2006, **178**, 42–55.
48 G. Li Manni, I. F. Galván, A. Alavi, F. Aleotti, F. Aquilante, J. Autschbach, *et al.*, The OpenMolcas Web: A Community-Driven Approach to Advancing Computational Chemistry, *J. Chem. Theory Comput.*, 2023, **19**, 6933–6991.
49 J. Huang, Q. Chen, Y. Ding, X. Zhu, B. Wang, F. Pan and Z. Zheng, Enhancement of Single–Molecule Magnet Properties by Manipulating Intramolecular Dipolar Interactions, *Adv. Sci.*, 2025, **12**, 2409730.
50 Y. C. Chen and M. L. Tong, Single-molecule magnets beyond a single lanthanide ion: the art of coupling, *R. Soc. Chem.*, 2022, **13**, 8716–8726.
51 (*a*) CCDC 2387470: Experimental Crystal Structure Determination, 2025, DOI: **10.5517/ccdc.csd.cc2l4c59**; (*b*) CCDC 2388164: Experimental Crystal Structure Determination, 2025, DOI: **10.5517/ccdc.csd.cc2l52kf**.